

# Early Material Damage in Equimolar CrMnFeCoNi in Mixed Oxidizing/Sulfiding Hot Gas Atmosphere

Anna Maria Manzoni,\* Wencke Mohring, René Hesse, Leonardo Agudo Jácome, and Christiane Stephan-Scherb

The challenges to use more varied fuels at medium and high temperatures above 500 °C need to be addressed by tuning the materials toward a better resistance against increased corrosion. As a first step the corrosion processes need to be better understood, especially in the case of the unavoidable and highly corrosive sulfur-based gases. Herein, oxidation/sulfidation of an equimolar CrMnFeCoNi high-entropy alloy is studied at an early stage after hot gas exposure at 600 °C for 6 h in 0.5% SO<sub>2</sub> and 99.5% Ar. The oxidation process is studied by means of X-ray diffraction, scanning and transmission electron microscopy, and supported by thermodynamic calculations. It is found that the sulfur does not enter the bulk material but interacts mainly with the fast-diffusing manganese at grain boundary triple junctions at the alloy surface. Submicrometer scaled Cr–S–O-rich phases close to the grain boundaries complete the sulfur-based phase formation. The grains are covered in different Fe-, Mn-, and Cr-based spinels and other oxides.

## 1. Introduction

Elevated temperatures in combination with reactive atmospheres (e.g., O<sub>2</sub>, CO<sub>2</sub>, H<sub>2</sub>O, SO<sub>2</sub>, etc.) may cause massive corrosion, leading to a change in safety-related properties. The need for energy sources other than fossil fuels has pushed the use of renewable fuels which are usually characterized by a much higher content of contaminants than, e.g., kerosene. A very common contaminating element both in renewable fuels and in heavy hydrocarbons used in the petrochemical industry is sulfur. Its combustion leads to the formation of corrosive gases, and materials in contact with them, even at low concentrations, are submitted to a potential loss of stability. Sulfur-containing


gases such as SO<sub>2</sub> and SO<sub>3</sub> are known to adversely affect corrosion rates and material loss of alloys in service at elevated temperatures. Thankfully the amount of sulfur in fuels has been strictly controlled over the last decade. Combined oxidation/sulfidation in this temperature regime has been intensively studied for steels,<sup>[1]</sup> ferritic,<sup>[2]</sup> and ferritic–martensitic materials.<sup>[3,4]</sup> These four references correspond to exemplarily studies that visualize the formation of an inner and outer corrosion layer in relation to the original alloy surface. The microstructure and phase composition of both layers strongly depend on the Cr content of the alloy. In ferritic alloys the outer corrosion layer, which is in contact with the gas atmosphere, consists mainly of iron oxides (hematite

Fe<sub>2</sub>O<sub>3</sub> and magnetite Fe<sub>3</sub>O<sub>4</sub>) because iron is the fastest of the diffusion elements.<sup>[5]</sup> The inner layer consists of (Fe,Cr)-mixed oxides of ((Fe,Cr)<sub>3</sub>O<sub>4</sub>) type.<sup>[6]</sup> Within both layers and even within the base alloy small precipitates (1–5 μm) of (Fe,Cr) sulfides, (Fe, Cr)<sub>x</sub>S<sub>y</sub>, are found frequently. It should be emphasized that in Cr-rich (9–16% Cr) alloys sulfidation of grain boundaries can be observed.<sup>[2,4,7,8]</sup> It is assumed that the sulfur diffuses through nondense, porous layers in both layers with micropores, cracks, and grain boundaries toward the oxide/alloy interface and induces a precipitation of sulfides. This phenomenon is called internal sulfidation or sulfide embrittlement and can affect the mechanical properties of an alloy. Cr sulfides at grain boundaries within a ferritic alloy with 13 wt% chromium were identified and reconstructed by transmission electron microscopy (TEM) and focused ion beam (FIB) serial slicing after exposure times of 3, 6, and 12 h.<sup>[7]</sup> It was shown that the sulfide precipitates have a higher hardness than the surrounding base alloy and the number of precipitates increased linearly, assuming a constant nucleation rate.

The materials used in sulfur containing conditions need to provide a better resistance to corrosion than those used with cleaner burning fuels, cleaner in the sense that they only consist of hydrocarbons. Next to the obvious addition of oxidation protective elements such as Cr and Al, a possible way of strengthening an alloy is the introduction of chemical diversity into the matrix material, i.e., providing a multielement phase instead of a solid solution that is based on one single main element. This approach has been well studied for dislocation movements (see, e.g., ref.[9] and the references therein), which are hindered by the solid solution compared to the single-based element alloy.

A. M. Manzoni, W. Mohring, R. Hesse, L. Agudo Jácome, C. Stephan-Scherb  
Bundesanstalt für Materialforschung und -prüfung  
12205 Berlin, Germany  
E-mail: anna.manzoni@bam.de

C. Stephan-Scherb  
Fachbereich Geowissenschaften  
Freie Universität Berlin  
12249 Berlin, Germany

 The ORCID identification number(s) for the author(s) of this article can be found under <https://doi.org/10.1002/adem.202101573>.

© 2022 The Authors. Advanced Engineering Materials published by Wiley-VCH GmbH. This is an open access article under the terms of the Creative Commons Attribution License, which permits use, distribution and reproduction in any medium, provided the original work is properly cited.

DOI: 10.1002/adem.202101573

The presence of several equally important elements may also reduce the interaction rate of corrosive elements such as O and S. High-entropy alloys (HEAs) can provide such a diversified matrix and are thus prime candidates to favor the formation of protective layers under aggressive atmospheres.

A single-phase material is thus the best choice for a comparative study and the HEA that has been chosen in this work is the well-studied equiatomic CrMnFeCoNi “Cantor” alloy. Many studies were conducted on its structure–property relationships in terms of phase stability, microstructure, strength, and ductility.<sup>[10–13]</sup> It shows excellent mechanical properties in terms of high ductility work hardening rate, ultimate tensile strength, and fracture toughness, especially at low temperatures, but it has also proven to show interesting oxidation behavior at higher temperatures around 600 °C.<sup>[14–16]</sup> Even though it will probably not be used in that temperature range, it can serve as a reference for many face-centered cubic (fcc) structured, Co–Cr–Fe–Ni-based HEAs that are designed for high-temperature applications such as high-entropy superalloys.<sup>[17]</sup> Until now, the focus of corrosion studies in the range of 500–800 °C has been on material behavior in laboratory or synthetic air,<sup>[14,15]</sup> and dry (2% O<sub>2</sub>) and humid (10% H<sub>2</sub>O) atmospheres<sup>[16]</sup> for exposure times of up to 100 h. All of these studies described fast growing porous Mn-rich oxides, leading to accelerated material degradation by corrosion.

The equimolar CrMnFeCoNi alloy contains not only a high amount of Cr but also of Mn and Fe which have high diffusion rates at temperatures around 600 °C.<sup>[18]</sup> In this context, the present study is motivated by the question whether and to what extent grain boundary sulfidation can be observed in CrMnFeCoNi after exposure to 0.5% SO<sub>2</sub> at 600 °C.

## 2. Results

### 2.1. Postexposure Surface Analysis

The oxidized HEA surface was characterized by scanning electron microscopy (SEM) (Figure 1a) and X-ray diffraction (XRD) (Figure 1b). After exposure to 0.5% SO<sub>2</sub> for 6 h at

600 °C, the fcc grain structure is still clearly visible, but the entire CrMnFeCoNi surface appears oxidized (Figure 1a). The grains, sized on average 50 μm in diameter,<sup>[16]</sup> reveal a gray oxide layer with dark gray precipitates (region 1). Along the grain boundaries, mainly dark gray (region 2, about 10 % in area) and partly white precipitates have formed. At triple points of the grain boundaries, large white precipitates containing cracks (region 3, about 1 % in area) grew in the form of triangles in the order of ≈20 μm. The three regions marked in Figure 1 will be investigated in detail through TEM investigations on lamellae cut by FIB in the regions of interest (Figures 2, 3 and 4).

The XRD patterns of the CrMnFeCoNi HEA exposed at 600 °C in 0.5% SO<sub>2</sub> for 6 h are shown in Figure 1b. The grazing incidence method only reveals the outermost layer, i.e., the spinel Fe<sub>2</sub>MnO<sub>4</sub>, in which Fe and Mn occupying the octahedral and tetrahedral sites in the lattice and oxygen are arranged in a cubic close-packed lattice.<sup>[19]</sup> The strongest peaks correspond to the substrate (fcc crystal structure) and occur at 2θ = 50.98°, 59.60°, and 89.42°. This is an indication that the oxide layer is thin, which correlates to the SEM surface image (Figure 1a), in which the microstructure is still visible.

### 2.2. Absence of Sulfides in the Depth of the Sample after Corrosion

Figure 2 shows an SEM back-scattered electron overview image over a TEM lamella extracted across a grain boundary similar to region 2 (see Figure 1a), highlighting two region of interest (ROIs) in which TEM (white) and SEM (blue) energy-dispersive X-ray spectroscopy (EDS) mappings were acquired. The SEM EDS elemental mappings show no traces of any sulfur accumulation in the bulk of the samples. Several pores under the surface of the targeted grain boundary can be distinguished and they induce edge effects in the C and O elemental mappings. One of the internal grain boundaries is decorated by Cr carbides, whose formation during production is hardly avoidable. Unlike previously studied Fe–Cr model alloys<sup>[20]</sup> that were exposed to the same atmosphere, the CrMnFeCoNi alloy shows no formation of metal sulfides along the grain boundaries.

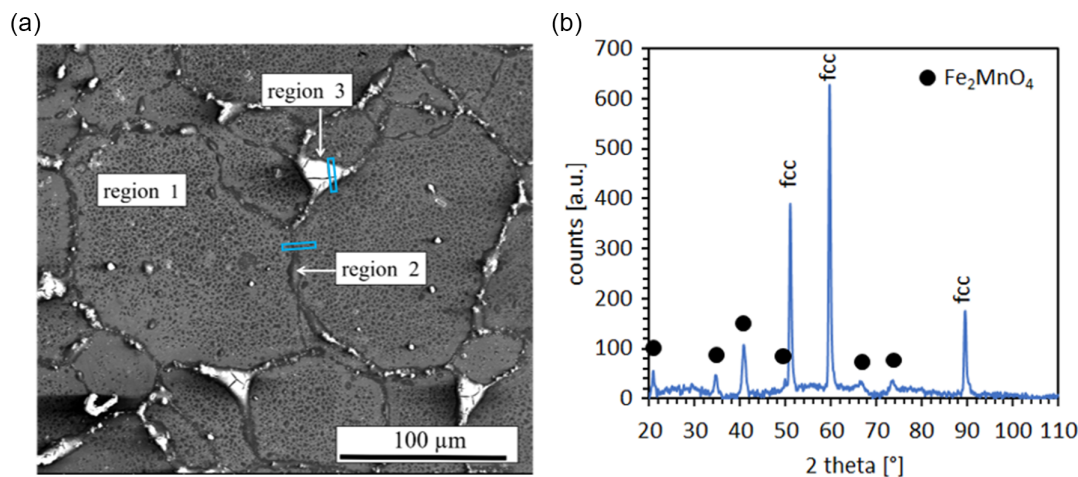


**Figure 1.** a) SEM image of the corroded HEA surface and b) X-ray diffractogram of the oxidized CrMnFeCoNi after exposure to 0.5% SO<sub>2</sub> at 600 °C for 6 h. The blue boxes correspond to areas similar to those where the TEM lamellae were cut.

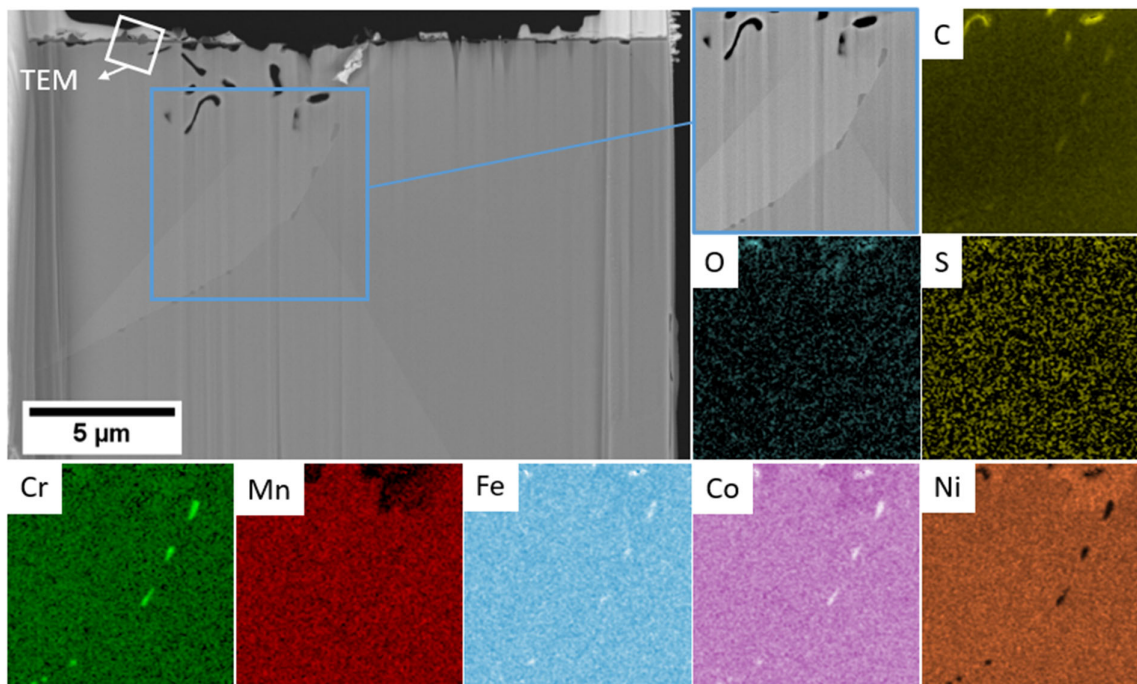


**Figure 2.** SEM BSE image of the TEM lamella of region 2, the blue box highlighting the region where the qualitative EDS elemental mappings of the five alloy elements and C, O, and S were taken along with an adjusted grey scale. The blue box highlights the position of the mappings. More intense color indicates a higher content of the element. Note that the mappings were acquired at 5 kV to highlight the light elements—quantitative deductions cannot be made here. The white box shows the region where the TEM EDS data were acquired.

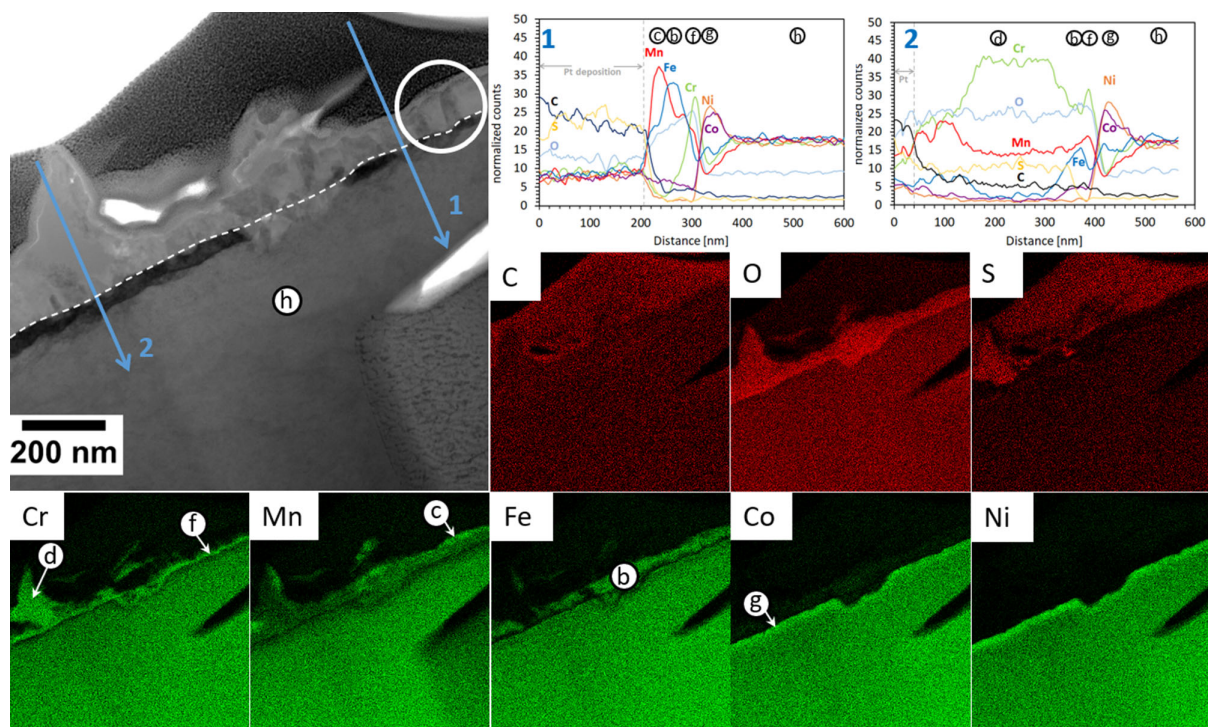


**Figure 3.** STEM BF from a region 2, line scans, and EDS elemental mappings of the five alloy elements and C, O, and S. The blue arrows highlight the position and orientation of the two line scans. The white circle indicates a region in the Mn–Fe oxide where the columnar growth is well visible. The white dashed line marks the limit between the last oxide and the bulk. Compositions in ①, ②, ③, ④, and ⑤ given in Table 1. Note that the line scans display the normalized counts, not at%.

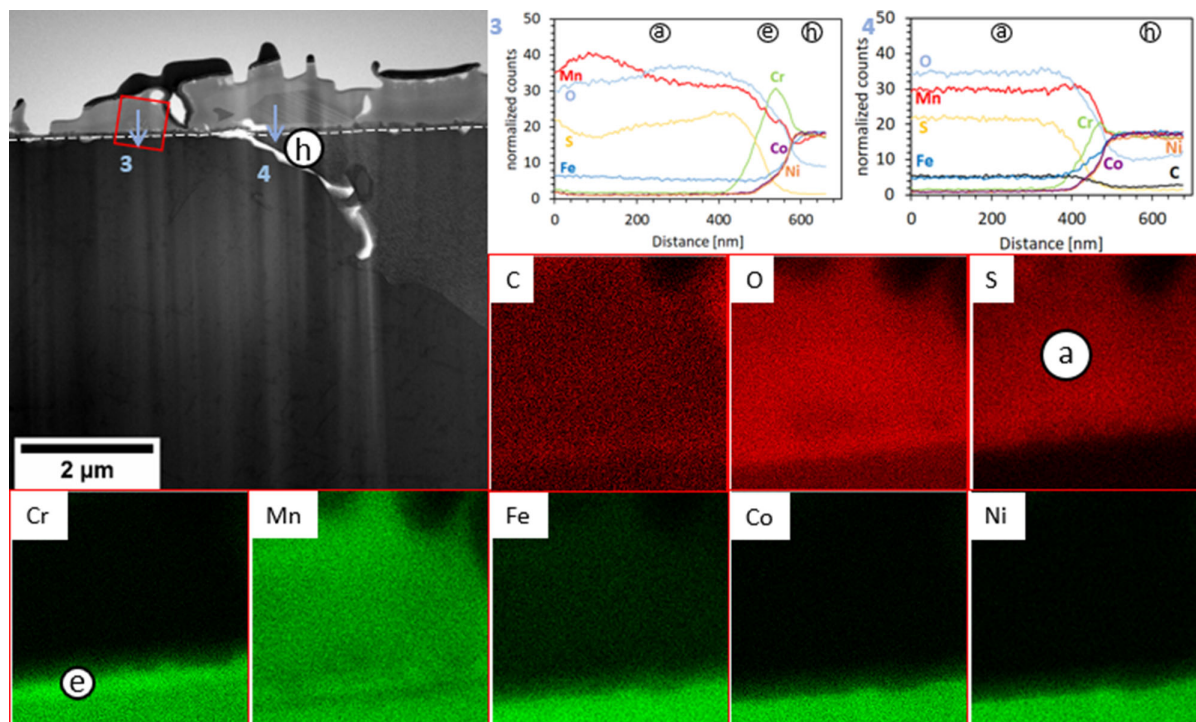


**Figure 4.** STEM BF image from a region 3, line scans, and EDS elemental mappings of the five alloy elements and C, O, and S. The blue arrows highlight the position and orientation of the two line scans labeled “3” and “4.” The red box indicates the area where the elemental mappings have been acquired. The white dashed line marks the limit between the last oxide and the bulk. Compositions in ①, ②, and ③ are given in Table 1. Note that the line scans display the normalized counts.

### 2.3. Oxidation Products along the Grain Boundaries and within the Grain

To what extent can grain boundary sulfidation be observed in CrMnFeCoNi after exposure to 0.5% SO<sub>2</sub> at 600 °C? The SEM overview image (see Figure 2) gave on a first glance no indication of grain boundary sulfidation. However, as can be seen in the SEM surface analysis (Figure 1), the change of the original surface is different at the center of the alloy grains from that at the grain boundaries. All compositions were determined by identifying and confining the ROI from the TEM EDS

elemental mappings and analyzing their spectra, the results of which are summarized in Table 1. All observed corrosion products and their localizations are summarized schematically in Figure 5.

#### 2.3.1. Regions 1 and 2

Figure 3 shows a scanning transmission electron microscopy (STEM) bright field (BF) image, two line scans (of regions 1 and 2) across the surface layers, and elemental distribution mappings of the five alloy elements and C, O, and S.

**Table 1.** Compositions of all phases as determined from the TEM EDS elemental mappings. The error bar corresponds to the standard deviation  $2\sigma$  and has been determined by the software. The real error is assumed to be considerably higher. Note that amounts for C and O are not reliable in a quantitative way.

In at%	C	O	S	Cr	Mn	Fe	Co	Ni
① Mn–S–O at triple GB	9.2 ± 4.7	9.6 ± 1.0	29.2 ± 3.3	2.4 ± 1.7	42.3 ± 5.6	1.2 ± 0.7	4.0 ± 0.9	2.1 ± 1.0
② Fe–Mn-rich oxide, Fe <sub>2</sub> MnO <sub>4</sub>	8.4 ± 0.5	3.7 ± 0.1	0.9 ± 0.2	3.3 ± 0.1	23.9 ± 0.3	42.6 ± 0.4	14.0 ± 0.5	3.2 ± 0.6
③ Mn–Fe-rich oxide	3.8 ± 1.0	3.3 ± 0.2	0.6 ± 0.4	1.6 ± 0.3	45.7 ± 1.2	27.1 ± 1.0	16.8 ± 1.9	1.4 ± 2.1
④ Cr–S particle	19.8 ± 0.8	4.1 ± 0.2	14.9 ± 0.5	42.4 ± 0.7	8.4 ± 0.3	3.0 ± 0.6	5.5 ± 0.8	1.8 ± 0.5
⑤ Cr(–Co–Ni)-rich	3.7 ± 0.1	2.2 ± 0.1	4.5 ± 0.1	25.2 ± 0.1	13.0 ± 0.1	13.0 ± 0.1	18.5 ± 0.1	20.0 ± 0.1
⑥ Cr-rich oxide	0.0	3.3 ± 0.1	0.7 ± 0.1	35.4 ± 0.6	12.8 ± 0.3	24.0 ± 0.9	19.1 ± 0.9	4.7 ± 0.5
⑦ Co–Ni rich	0.0	0.0	0.0	7.9 ± 0.3	4.0 ± 0.2	14.1 ± 0.4	30.1 ± 0.7	43.9 ± 1.0
⑧ Bulk (close to surface)	5.7 ± 0.3	0.2 ± 0.0	0.1 ± 0.1	11.4 ± 0.3	9.0 ± 0.9	17.4 ± 0.1	24.5 ± 0.5	31.7 ± 0.5

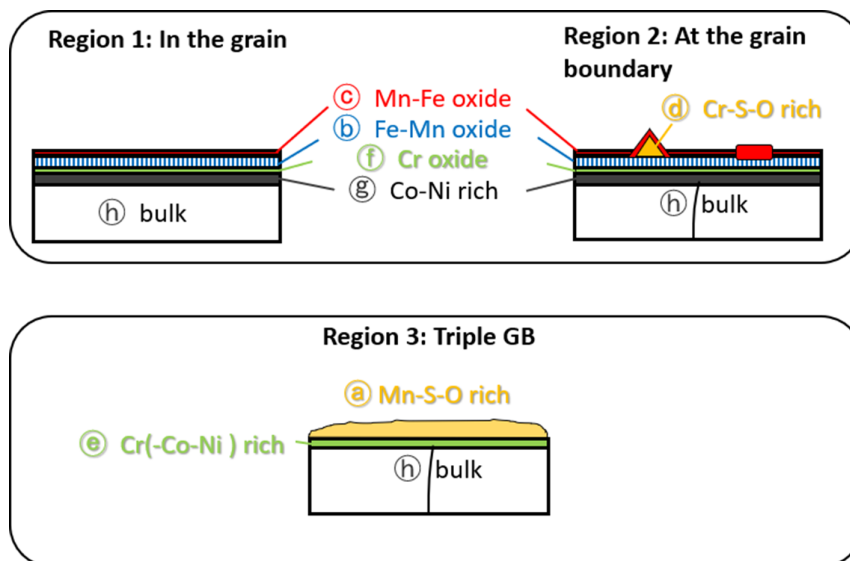


**Figure 5.** Schematic view of the layers that formed on the CrMnFeCoNi alloy after the corrosion at 600 °C.

### 2.3.2. Region 1 (Line Scan 1)

The outermost, interrupted layer at the gas interface is about  $20 \pm 5$  nm thick and rich in Mn and O (marked by © in the Mn map). It is neighbored by an about  $50 \pm 20$  nm-thick Fe(-Mn)-rich oxide (Ⓞ in the Fe map), whose composition corresponds to the  $\text{Fe}_2\text{MnO}_4$  detected by XRD (Figure 1b). This oxide layer grows in columnar grains as is highlighted in the white circle in Figure 3. The oxide closest to the bulk alloy is rich in Cr and about  $20 \pm 5$  nm wide (see ⓕ in the Cr map). The outermost part of the bulk is characterized by a clearly distinguishable increase in Co and Ni at the cost of Fe, Cr, and Mn (see Ⓢ in the Co map). This region shows a black contrast in the STEM BF, even though it shows the same crystal structure as the bulk material (disordered fcc). This increase in Ni and Co is indeed a depletion in Cr, Mn, and Fe, all of which have higher diffusion rates than Ni and Co at this temperature.<sup>[18]</sup> A similar phenomenon has been reported in CoCrNi.<sup>[21]</sup> Below the Co-Ni enriched region, the alloy slowly regains its nominal composition (see Ⓢ in the STEM BF image).

### 2.3.3. Region 2 (Line Scan 2)

Line scan 2 shows an additional region which is characterized by a size of about 250 nm in diameter and an enrichment in Cr, O, and S (ⓐ in the Cr map). It is locally neighbored by an about  $40 \pm 10$  nm-thick Mn(-Cr)-rich oxide. These submicrometer-sized particles are quite scarce on the surface of the TEM sample and are too small to be resolved in the SEM image (Figure 1).

Below the Cr-S-O-rich particle (ⓐ), the Cr-rich oxide (ⓕ) and the Co-Ni enriched region of the bulk (Ⓢ) can be observed. Note that neither the Mn oxide (©) nor the Fe(-Mn)-rich oxide (Ⓞ) from region 1 can be distinguished here.

### 2.3.4. Region 3

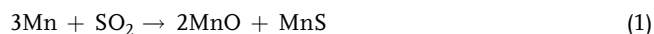
Figure 4 shows a STEM BF image of a TEM lamella that was extracted from an area similar to region 3 (see Figure 1), along with two line scans (along the blue arrows “3” and “4”) and elemental distribution mappings of C, O, S, and the five alloy elements that were acquired in the area marked with a red box. The two line scans start in the large precipitates at the grain boundary triple junction (see Figure 1) which are enriched in Mn, S, and O (ⓐ). Variations in the Mn, S, and O counts in line scan 3 are mirrored by rather large error bars given in Table 1. Unlike in regions 1 and 2, there is not a remarkable variety in oxide layers. Under the Mn-S phase a Cr-O-rich region can be distinguished (see ⓕ in the Cr map, Figure 4), but its composition is different from that in regions 1 and 2 (see ⓕ in Figure 3)—it has a much higher content in Co and Ni and even a certain amount of S. There is also no region with a distinguished increase in Co and Ni, unlike the one present in regions 1 and 2 (see Ⓢ in Figure 3). A slight enrichment in Co and Ni can be found in the bulk close to the original alloy surface and this area has the same composition as the corresponding area in regions 1 and 2 (see Ⓢ in the STEM BF image in Figure 4).

## 2.4. Impact on the Material Degradation

### 2.4.1. $\text{SO}_2$ —The Corrosive Gas

The most remarkable feature observed in this study is the phase enriched in Mn, S, and O (see ⓐ in Figure 4) that was formed at the grain boundary triple junctions (region 3). It could either be a duplex layer consisting of  $\text{MnO} + \text{MnS}$  or a manganese sulfate ( $\text{MnSO}_4$ ). Several authors<sup>[22–25]</sup> described the corrosion behavior of pure manganese and Mn containing alloys in  $\text{SO}_2$  at

$T \geq 600$  °C, in which the phases MnO and MnS were the corrosion products. Gesmundo et al.<sup>[22]</sup> investigated the corrosion behavior of pure manganese (99.97%) in pure SO<sub>2</sub> (99.98%) at 700, 800, and 900 °C for 2, 4, and 6 h each. Independent of temperature and reaction time, the grown corrosion layers exhibited the same phase composition and structure consisting of a fine-grained mixed layer at the oxide/alloy interface (MnO and MnS), an intermediate duplex layer (coarse sulfide particles irregularly arranged in a MnO matrix), and a pure MnO layer in contact with the gas. Thermodynamic calculations have shown that MnO is the stable phase during corrosion in 1 atm SO<sub>2</sub>. Higher manganese oxides (3-, 4-, etc.) cannot form because of the low oxygen partial pressure. The formation of a MnO/MnS layer occurs when the gas phase reacts directly with the manganese surface according to Equation (1)



Here, it is assumed that this reaction takes place especially at the surface of the alloy grain boundaries (see Figure 4), where outward diffusion of manganese is expected to be fast. Because of its high diffusivity and affinity for oxidation, manganese diffuses from the bulk and especially along the grain boundaries and reacts directly with the SO<sub>2</sub>, resulting in the formation of white precipitates (Figure 1a, region 3) composed of a duplex layer MnO/MnS according to Equation (1). Related to this, thermodynamic calculations using Factsage (Figure 6) also indicate that MnO and MnS are the stable phases on CrMnFeCoNi during the exposure in 0.5% SO<sub>2</sub> at 600 °C (Figure 6a, yellow dashed line). Figure 6b presents the thermochemical diagram for Mn–O–S related to McAdam and Young<sup>[24]</sup> and fitted to 600 °C with Factsage-Equilib. With a  $p_{\text{O}_2} = 1.9871 \times 10^{-36}$  atm and a  $p_{\text{S}_2} = 1.3726 \times 10^{-24}$  atm, both phases, MnO and MnS, are stable simultaneously. Low sulfur partial pressures encourage the formation of stable metal oxides. If the partial pressures of sulfur and oxygen are low, the metal remains stable. In case of high  $p_{\text{O}_2}$  and  $p_{\text{S}_2}$ , sulfates would be the stable phases.

It has been shown previously that CrMnFeCoNi has a poor oxidation resistance in air,<sup>[14,15]</sup> in O<sub>2</sub> and in H<sub>2</sub>O<sup>[16]</sup> atmospheres at high temperatures, due to the fast growth of porous Mn-rich oxide layers. The oxide layers in the study by Stephan-Scherb et al.<sup>[16]</sup>

mainly consisted of Mn<sub>3</sub>O<sub>4</sub> and  $\alpha$ -Mn<sub>2</sub>O<sub>3</sub>. In the present study, MnO was observed. The differences in type and structure of the manganese oxide observed can mainly be explained by the low oxygen partial pressure  $p_{\text{O}_2}$ . When comparing different past studies, it can be concluded that the observed phases Mn<sub>3</sub>O<sub>4</sub> and Mn<sub>2</sub>O<sub>3</sub> are stable at much higher  $p_{\text{O}_2}$ , e.g.,  $p_{\text{O}_2} = 0.02$  atm and 10–7 atm in the study by Stephan-Scherb et al.,<sup>[16]</sup> compared to the  $p_{\text{O}_2} = 2 \times 10^{-36}$  atm used in this study. However, the high diffusivity of manganese and its affinity for oxidation dominates the oxidation and corrosion process. Marasco and Young<sup>[26]</sup> analyzed the oxidation of FeCrMn alloys with varying Mn and Cr contents (2, 6, and 10 wt% Mn and 5, 12, and 20 wt% Cr) at 900 °C with an oxygen partial pressure of  $p_{\text{O}_2} = 0.2$  atm. In these alloys, even the large amount of Cr could not prevent the formation of fast growing (Fe, Cr, Mn)<sub>3</sub>O<sub>4</sub> spinels where the formation of chromia would be beneficial. In the present study, lower oxygen partial pressures of  $p_{\text{O}_2} = 2 \times 10^{-36}$  atm were employed and they also resulted in the formation of fast growing transient Mn-rich oxides in CrMnFeCoNi. As manganese oxides are observed already after 6 h of exposure, it is expected that the alloy performs poorly in terms of long-time stability in an atmosphere containing 0.5% SO<sub>2</sub>.

#### 2.4.2. Comparison of CrMnFeCoNi to Other Alloys Submitted to SO<sub>2</sub>

Compared to a previous study on Fe–13Cr (wt%),<sup>[2]</sup> the sulfur impact on the material degradation of the HEA is restricted to the areas very close to the surface. No diffusion of S into the material could be observed, neither in the grains nor at the grain boundaries. Instead, about 1 % of the surface area is covered in a large Mn–S–O-rich phase. The submicrometer-sized Cr–S–O-rich phases can probably be neglected at this point. This observation implies that, unlike in Fe–13Cr, there is no inward diffusion of S but instead an outward diffusion of Mn. Mn is known to be a fast-diffusing element, and this is even more the case in the CrMnFeCoNi alloy, as shown recently by Gärtner et al.<sup>[18]</sup> Compared to the other elements, Mn can cover the greatest distances at 600 °C. Figure 7 compares the maximum diffusion paths of the five alloying elements in several bulk alloys and compounds, not considering the grain boundary diffusion. The paths were calculated using the Arrhenius equation

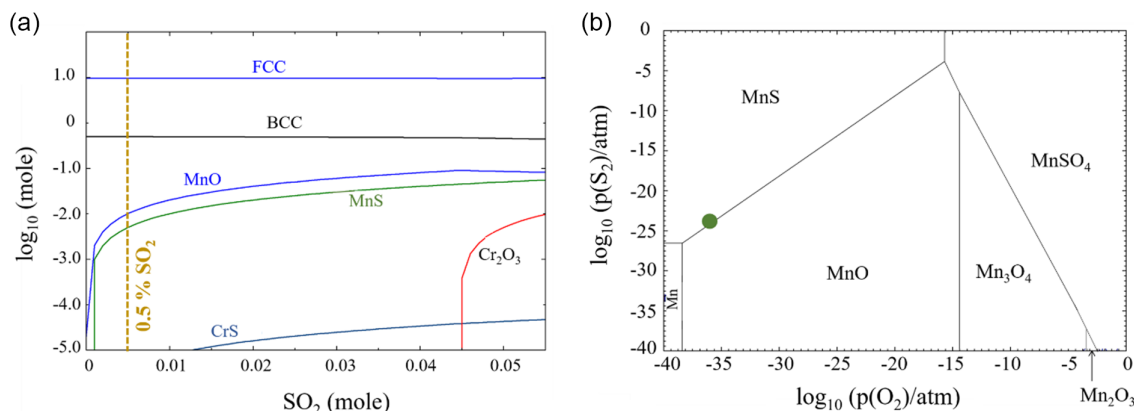


**Figure 6.** a) Stability diagram of CrMnFeCoNi in SO<sub>2</sub> up to 5% and b) thermochemical diagram for Mn–O–S (Factsage). The green dot in the stability diagram indicates the equilibrium S<sub>2</sub> and O<sub>2</sub> pressure in the system SO<sub>2</sub>(g) and the “Cantor alloy”.

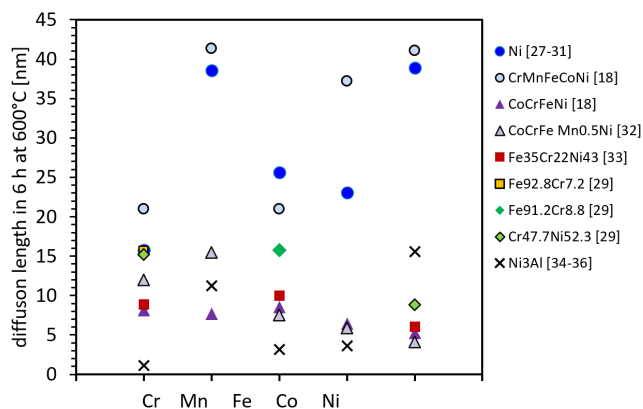


**Figure 7.** Maximum diffusion paths of the five alloying elements in different bulk media at 600 °C for 6 h.

$$D = D_0 \exp\left(-\frac{Q}{RT}\right) \quad (2)$$

and the relationship between the diffusion coefficient  $D$  and the diffusion path  $x$

$$x = \sqrt{D \cdot t} \quad (3)$$

with  $D_0$  being the preexponential factor,  $Q$  the activation energy,  $R$  the universal gas constant,  $T$  the temperature, and  $t$  the time. Data for calculation were taken from previous studies.<sup>[18,27–36]</sup>

The speed of Mn allows the element to react with S at the surface of the alloy and to form MnS and MnO according to Equation (1). This process is equivalent to that of Fe in pure Fe or steels with only little Cr as has been shown by Nützmänn et al.<sup>[2]</sup> For the other pure elements, i.e., Cr, Mn, Co, and Ni in a pure SO<sub>2</sub> atmosphere at  $T > 500$  °C, it was also underlined that mixed oxides composed of MO and MS (M = Cr, Mn, Co, Ni) are formed in any case.<sup>[24,37–40]</sup>

It is worth noting that the mixed MnS–MnO formation after 6 h of exposure mainly proceeds at the grain boundaries, whereas the grain center is covered by Fe<sub>2</sub>MnO<sub>4</sub>. As Figure 7 displays only bulk diffusion, the diffusion lengths displayed there reflect the expected layer structure at the surface of the grain. Mn enrichment was observed at the oxide/gas interface (see Figure 3) followed by Cr and Fe enriched oxides at the oxide/alloy interface. However, from Figure 7, Ni and Co are expected to be as fast as Mn and to contribute more to the oxidation than Cr and Fe. But this is not the case. Fe- and Cr-rich oxides are observed at the oxide/alloy interface. This might be explained by the lower Gibb's free energy for the oxidation of Fe and Cr compared to that of Ni and Co. This behavior reflects the fact that high-temperature oxidation and corrosion is always a complex interplay between thermodynamics and kinetics and different for different classes of materials and atmospheres applied.

### 3. Conclusion

In this study, on the influence of SO<sub>2</sub> on the CrMnFeCoNi “Cantor” alloy it was found that the corrosive element sulfur,

which is omnipresent in renewable fuels, has only a small effect at the alloy surface. About 1% of the surface area, situated at the grain boundary triple junctions, is covered in a Mn–S–O-rich precipitate that consists of MnS and MnO when the alloy is aged at 600 °C for 6 h. A small amount of Cr–S–O-rich precipitates are formed inside the grains. The greatest part of corrosion products is Mn-, Fe-, and Cr-rich oxides that form throughout the surface with a total corrosion scale thickness of about 200 nm. Even though there is no S penetration into the material, which is a good sign for its corrosion resistance, the presence of unstable Mn oxides after this short aging time at a medium temperature is indicative for nonprotective behavior at longer exposure times.

### 4. Experimental Section

**Material Preparation and Corrosion Procedure:** The equimolar CrMnFeCoNi alloy was prepared by melting the raw elements in a vacuum induction melting furnace (Leybold Heraeus IS 1/III) starting with high purity metals ( $\geq 99.9\%$  by weight). In order to prevent oxidation and evaporation of the elements during melting and casting, the chamber of the furnace was evacuated to 3 mbar prior to melting and then filled with Ar to a pressure of 500 mbar. After melting and casting, the resulting ingots ( $\approx 2$  kg) were turned on a lathe to reduce their diameter from 45 to 40 mm. Homogenization of the ingots took place in sealed and evacuated quartz tubes ( $p = 3 \times 10^{-5}$  mbar) at 1200 °C for 48 h. After homogenization, the diameter of the ingots was reduced from 40 to 17 mm by rotary swaging at room temperature. The alloys were finally recrystallized to an average grain size of  $\approx 50$   $\mu$ m by heat treatment for 1 h at 1020 °C. More details about alloy preparation can be found elsewhere.<sup>[41,42]</sup> The alloy composition has been verified by electron probe microanalyzer, as has been reported in the study by Stephan-Scherb et al.<sup>[16]</sup>

Samples for corrosion tests were cut to 3 mm-thick disks and then ground with abrasive paper down to a grit size of 1200.

Short time gas exposure in 0.5% SO<sub>2</sub>/99.5% Ar was conducted in a tailor-made reaction chamber at 600 °C for 6 h. Fast heating was realized by an infrared radiant heater. Fast cooling was realized by water cooling built into the steel lid, allowing the analysis of the corrosion products in an as-frozen state. Samples were positioned parallel to the gas flow and joined by a thermocouple to allow an exact temperature control. Heating up to 600 °C and cooling down to room temperature was achieved under pure Ar flow. For more information on the furnace, the reader is referred to previous studies.<sup>[2,20]</sup>

The TEM lamella was prepared in a FIB microscope by FEI, i.e., a Quanta 3D FEG-SEM/FIB. The lamella was first thinned with a beam of 30 kV energy and final polishing was done at 2 kV.

**Characterization Methods:** XRD was performed in a Seifert XRD 3000 PTS at grazing incidence geometry. The wavelength used for experiments was Co K $\alpha$ .

Two scanning electron microscopes (SEM) were used in this study. The first is a Zeiss Gemini 1530 equipped with an EDS detector by ThermoFisher and the EDS software NSS. The voltage used for EDS mappings was 5 keV to highlight the light elements. The second SEM is part of the FIB FEI Quanta, operated at 20 kV.

The TEM used in this study is a JEOL JEM 2200FS equipped with a field emission gun, an in-column energy filter as well as BF and high-angle annular dark field detectors for the scanning (S)TEM mode. The TEM was operated at an acceleration voltage of 200 kV and is equipped with an EDS JED-2300 detector (JEOL). EDS line scans were extracted from the elemental mappings and smoothed using the Savitzky–Golay method<sup>[43]</sup> over ten points. Quantitative measurements were extracted from the corresponding regions in the elemental mappings and calculated using the PRZ method.<sup>[44]</sup>

Thermodynamic equilibrium calculations for phase stability under the applied atmosphere were performed with Factsage 7.0<sup>[45]</sup> using the FactPS

and Factoid databases. The ImageJ software<sup>[46]</sup> along with a trainable Weka segmentation<sup>[47]</sup> was used for the determination of area fractions.

## Acknowledgements

The authors thank the German Research Foundation (DFG) for the financial support through MA7004-2 and project number 398838389, and through the Priority Program SPP2006 "Compositionally Complex Alloys-High Entropy Alloys (CCA-HEA)." Many thanks to the supporting colleagues: to Hennig Goldbeck for help with XRD measurements, to Axel Kranzmann for the thermodynamic calculations, to Daniel Abou-Ras from HZB for SEM discussions and the use of his Gemini, to Guillaume Laplanche for providing the material, and to Robert Maaß and Franziska Emmerling for support and motivation.

Open access funding enabled and organized by Projekt DEAL.

## Conflict of Interest

The authors declare no conflict of interest.

## Data Availability Statement

The data that support the findings of this study are available from the corresponding author upon reasonable request.

## Keywords

high-entropy alloys, high-temperature corrosion, MnO–MnS, oxidation, sulfidation

Received: November 15, 2021

Revised: January 11, 2022

Published online:

- [1] Z. Żurek, J. Gilewicz-Wolter, M. Hetmańczyk, J. Dudała, A. Stawiarski, *Oxid. Met.* **2005**, *64*, 379.
- [2] K. Nützmann, A. Kranzmann, C. Stephan-Scherb, *Mater. High Temp.* **2018**, *35*, 558.
- [3] P. Huczukowski, T. Olszewski, M. Schiek, B. Lutz, G. R. Holcomb, V. Shemet, W. Nowak, G. H. Meier, L. Singheiser, W. J. Quadackers, *Mater. Corros.* **2014**, *65*, 121.
- [4] K. Chandra, A. Kranzmann, R. Saliwan Neumann, G. Oder, F. Rizzo, *Oxid. Met.* **2015**, *83*, 291.
- [5] M. G. C. Cox, B. McEnaney, V. D. Scott, *Philos. Mag.: A J. Theor. Exp. Appl. Phys.* **1972**, *26*, 839.
- [6] K. Weber, A. Guilherme Buzanich, M. Radtke, U. Reinholz, C. Stephan-Scherb, *Mater. Corros.* **2019**, *70*, 1360.
- [7] K. Nützmann, N. Wollschläger, C. Rockenhäuser, A. Kranzmann, C. Stephan-Scherb, *JOM* **2018**, *70*, 1478.
- [8] J. Hucinska, *Adv. Mater. Sci.* **2006**, *6*, 16.
- [9] A. M. Manzoni, U. Glatzel, *Mater. Charact.* **2019**, *147*, 512.
- [10] A. Gali, E. P. George, *Intermetallics* **2013**, *39*, 74.
- [11] B. Gludovatz, A. Hohenwarter, D. Catoor, E. H. Chang, E. P. George, R. O. Ritchie, *Science* **2014**, *345*, 1153.
- [12] Z. Wu, H. Bei, G. M. Pharr, E. P. George, *Acta. Mater.* **2014**, *81*, 428.
- [13] G. Laplanche, J. Bonneville, C. Varvenne, W. A. Curtin, E. P. George, *Acta. Mater.* **2018**, *143*, 257.
- [14] G. Laplanche, U. F. Volkert, G. Eggeler, E. P. George, *Oxid. Met.* **2016**, *85*, 629.
- [15] G. R. Holcomb, J. Tylczak, C. Carney, *JOM* **2015**, *67*, 2326.
- [16] C. Stephan-Scherb, W. Schulz, M. Schneider, S. Karafiludis, G. Laplanche, *Oxid. Met.* **2021**, *95*, 105.
- [17] T. K. Tsao, A. C. Yeh, C. M. Kuo, K. Takehi, H. Murakami, J. W. Yeh, S. R. Jian, *Sci. Rep.* **2017**, *7*, 9.
- [18] D. Gaertner, J. Kottke, Y. Chumlyakov, F. Hergemoller, G. Wilde, S. V. Divinski, *Scr. Mater.* **2020**, *187*, 57.
- [19] M. Goodarz Naseri, E. B. Saion, A. Kamali, *ISRN Nanotechnol.* **2012**, *2012*, 604241.
- [20] C. Stephan-Scherb, M. Menneken, K. Weber, L. A. Jácome, G. Nolze, *Corros. Sci.* **2020**, *174*, 108809.
- [21] M. P. Agustianingrum, U. Lee, N. Park, *Corros. Sci.* **2020**, *173*, 108755.
- [22] F. Gesmundo, C. Deasmundis, C. Bottino, *Oxid. Met.* **1980**, *14*, 15.
- [23] B. Gillot, M. Radid, *Oxid. Met.* **1990**, *33*, 279.
- [24] G. McAdam, D. J. Young, *Oxid. Met.* **1992**, *37*, 301.
- [25] G. McAdam, D. J. Young, *Corros. Sci.* **1996**, *38*, 247.
- [26] A. L. Marasco, D. J. Young, *Oxid. Met.* **1991**, *36*, 157.
- [27] R. A. Swalin, A. Martin, in *AIME Transactions*, Vol. 206, American Institute of Mining Engineers, New York City **1956**, p. 567, Ch. 567.
- [28] A. Hässner, W. Lange, *Phys. Status Solidi B* **1965**, *8*, 77.
- [29] J. Růžičková, B. Million, *Mater. Sci. Eng.* **1981**, *50*, 59.
- [30] H. Bakker, J. Backus, F. Waals, *Phys. Status Solidi B* **1971**, *45*, 633.
- [31] K. Monma, H. Suto, H. Oikawa, *J. Jpn. Inst. Met.* **1964**, *28*, 188.
- [32] K. Y. Tsai, M. H. Tsai, J. W. Yeh, *Acta. Mater.* **2013**, *61*, 4887.
- [33] S. J. Rothman, L. J. Nowicki, G. E. Murch, *J. Phys. F: Met. Phys.* **1980**, *10*, 383.
- [34] C. Cserhati, A. Paul, A. A. Kodentsov, M. J. H. van Dal, F. J. J. van Loo, *Intermetallics* **2003**, *11*, 291.
- [35] Y. Minamino, S. B. Jung, T. Yamane, K. Hirao, *Metall. Trans. A* **1992**, *23*, 2783.
- [36] S. B. Jung, Y. Minamino, H. Araki, T. Yamane, K. Hirao, S. Saji, *Defect Diffus. Forum* **1993**, *95–98*, 859.
- [37] C. De Asmundis, F. Gesmundo, C. Bottino, *Oxid. Met.* **1980**, *14*, 351.
- [38] F. Gesmundo, C. de Asmundis, P. Nanni, *Oxid. Met.* **1983**, *20*, 217.
- [39] P. Kofstad, G. Åkesson, *Oxid. Met.* **1978**, *12*, 503.
- [40] P. Singh, N. Birks, *Oxid. Met.* **1978**, *12*, 23.
- [41] G. Laplanche, S. Berglund, C. Reinhart, A. Kostka, F. Fox, E. P. George, *Acta. Mater.* **2018**, *161*, 338.
- [42] M. Schneider, E. P. George, T. J. Manescau, T. Zálezák, J. Hunfeld, A. Dlouhý, G. Eggeler, G. Laplanche, *Int. J. Plast.* **2020**, *124*, 155.
- [43] A. Savitzky, M. J. E. Golay, *Anal. Chem.* **1964**, *36*, 1627.
- [44] J. L. Pouchou, F. Pichoir, in *Electron Probe Quantitation*, (Eds: K. F. J. Heinrich, D. E. Newbury), Springer, Springer, Boston, MA **1991**.
- [45] C. W. Bale, E. Bélisle, P. Chartrand, S. A. Decterov, G. Eriksson, A. E. Gheribi, K. Hack, I. H. Jung, Y. B. Kang, J. Melançon, A. D. Pelton, S. Petersen, C. Robelin, J. Sangster, P. Spencer, M. A. Van Ende, *Calphad* **2016**, *54*, 35.
- [46] C. A. Schneider, W. S. Rasband, K. W. Eliceiri, *Nat. Methods* **2012**, *9*, 671.
- [47] I. Arganda-Carreras, V. Kaynig, C. Rueden, K. W. Eliceiri, J. Schindelin, A. Cardona, H. S. Seung, *Bioinformatics* **2017**, *33*, 2424.